

PROCEEDINGS OF SPIE

SPIDigitalLibrary.org/conference-proceedings-of-spie

Joint synthesis of WMn MPRAGE and parameter maps using deep learning and an imaging equation

Pouria Tohidi, Shuo Han, Lianrui Zuo, Jiachen Zhuo, Steven Roys, et al.

Pouria Tohidi, Shuo Han, Lianrui Zuo, Jiachen Zhuo, Steven R. Roys, Aaron Carass, Rao P. Gullapalli, Jerry L. Prince, "Joint synthesis of WMn MPRAGE and parameter maps using deep learning and an imaging equation," Proc. SPIE 12464, Medical Imaging 2023: Image Processing, 124642F (3 April 2023); doi: 10.1117/12.2653988

SPIE.

Event: SPIE Medical Imaging, 2023, San Diego, California, United States

Joint Synthesis of WMn MPRAGE and Parameter Maps Using Deep Learning and an Imaging Equation

Pouria Tohidi^a, Shuo Han^b, Lianrui Zuo^{a,c}, Jiachen Zhuo^d, Steven R. Roys^d,
Aaron Carass^a, Rao P. Gullapalli^d, and Jerry L. Prince^{a,b}

^aDepartment of Electrical and Computer Engineering,
Johns Hopkins University, Baltimore, MD 21218

^bDepartment of Biomedical Engineering,
Johns Hopkins School of Medicine, Baltimore, MD 21205

^cLaboratory of Behavioral Neuroscience, National Institute on Aging,
National Institutes of Health, Baltimore, MD 20892

^dDepartment of Diagnostic Radiology and Nuclear Medicine,
University of Maryland School of Medicine, Baltimore, MD 21201

ABSTRACT

T1-weighted (T1w) magnetic resonance (MR) neuroimages are usually acquired with an inversion time that nulls the cerebrospinal fluid—i.e., CSFn MPRAGE images—but are rarely acquired with the white matter nulled—i.e., WMn images. Since WMn images can be useful in highlighting thalamic nuclei, we develop a method to synthesize these images from other images that are often acquired. We propose a two-part model, with a deep learning based encoder and a decoder based on an imaging equation which governs the acquisition of our T1w images. This model can be trained on a subset of the dataset where the WMn MPRAGE images are available. Our model takes image contrasts that are often acquired (e.g., CSFn MPRAGE) as input, and generates WMn MPRAGE images as output, along with two quantitative parameter maps as intermediate results. After training, our model is able to generate a synthetic WMn MPRAGE image for any given subject. Our model results have high signal-to-noise ratio and are visually almost identical to the ground truth images. Furthermore, downstream thalamic nuclei segmentation on synthetic WMn MPRAGE images are consistent with ground truth WMn MPRAGE images.

Keywords: Synthetic multi-TI, MRI synthesis, WMn MPRAGE, imaging equation, paired preprocessing, quantitative MRI, thalamic nuclei

1. INTRODUCTION

The thalamus is an important subcortical structure that has been described as “the gateway to the cortex”.¹ The thalamic nuclei, however, are not readily distinguished in standard T1-weighted magnetic resonance (MR) images—i.e., magnetization-prepared rapid gradient echo (MPRAGE) images—due to insufficient contrast.² Standard MPRAGE images are designed to null the cerebrospinal fluid (CSF), which tends to improve the contrast between gray matter and white matter; these images can be termed CSF-nulled (CSFn) MPRAGE images. In contrast, white matter nulled (WMn) MPRAGE images (also called fast gray matter acquisition T1 inversion recovery or FGATIR³ images) have been shown to better reveal the thalamic nuclei.^{3,4} Contrast-weighted MR images, as acquired and used in clinical settings, are of a qualitative nature. However, using the appropriate equations, one can extract quantitative parameter maps from such images. These parameter maps can be used together with imaging equations to generate synthetic contrast-weighted MR images with arbitrary acquisition

Further author information: (Send correspondence to Pouria Tohidi)
Pouria Tohidi: E-mail: pouria.tohidi.g@jhu.edu

parameters.^{5,6} Given two T1w images with similar acquisition protocols but different inversion times, one can solve a system of two equations per voxel to calculate proton density (PD) and T1 parameter maps, which can be used to synthesize T1w images with an arbitrary inversion time (TI). In particular, WMn MPRAGE images when acquired in conjunction with CSFn MPRAGE images allow us to compute multi-TI (MTI) T1w images based on approximations of the imaging equations for MPRAGEs; these multi-TI images have also been shown to highlight different thalamic nuclei for different values of TI.² WMn MPRAGE images are not typically acquired in conventional clinical imaging protocols⁷ and they may not be available for all subjects in a dataset. Our aim is to develop a method to synthesize WMn MPRAGE images from other available images so that they can be used in combination with the more traditionally acquired CSFn MPRAGE to segment the whole thalamus and parcellate the thalamic nuclei.

In contrast to the equation-based synthesis approaches, deep learning methods use examples to find relationships between images of different contrast and thereby creates direct synthesis methods. Two recent methods are particularly relevant to the work described in this paper. First, the method reported in Umaphathy et al.⁷ uses a single CSFn MPRAGE image to directly synthesize a WMn MPRAGE image using a deep network. Our work differs from this work in that we use multiple images to synthesize a WMn MPRAGE image and we also incorporate a generic imaging equation that relates the CSFn and WMn images. Second, the method in Moya-S  ez et al.⁸ computes T1, T2, and PD parametric maps using just two weighted images. We also compute parametric maps, but our method can incorporate additional acquired images as input, is trained from actual rather than synthetic images, and is specifically targeted to the synthesis of WMn MPRAGE images and MTI images.

In this paper, we propose a method based on deep learning (DL) and an imaging equation, which can be trained to take as input multiple images of different contrasts, and outputs a WMn MPRAGE image as well as a PD map and a T1 map. The same equation can then be used on the parameter maps to generate synthetic MTI T1w images. We evaluate the output of our method in two experiments. Our method improves upon the two aforementioned works as 1) it incorporates the imaging equation into the synthesis model, and 2) it is supervised by qualitative contrast-weighted images in an end-to-end manner. The former enables the model to synthesize quantitative parameter maps (PD and T1 maps) as intermediate values, which is an improvement over the work of Umaphathy et al.,⁷ as our method enables flexible image synthesis with given acquisition parameters. The latter allows us to train the model using only contrast-weighted images and without the need for parameter maps to be derived from the acquired images beforehand, an advantage of our work over Moya-S  ez et al.,⁸ as it decreases the computation required during preprocessing of the acquired images. To our knowledge, this is the first work to combine DL and imaging equations for end-to-end T1w MRI synthesis, and the first to perform paired preprocessing to preserve the relative intensities of two images, as we describe in detail in Sec. 2.3.

2. DATA AND METHODS

2.1 Data

We acquired four MR tissue contrast neuroimages on 18 subjects: 1) T1w (CSFn) MPRAGE, 2) T1w WMn MPRAGE, 3) T2w, and 4) T2w fluid attenuated inversion recovery (T2-FLAIR). Examples of the MR tissue contrasts that we collected are shown in Fig. 1, as well as example outputs from our processing. The first two images were acquired using identical sequences except for their TIs, which were 1,400 ms and 400 ms, respectively. The repetition time (TR) was set to 4,000 ms for both sequences. Throughout this paper, we often refer to the first image as an MPRAGE image (omitting the CSFn qualifier) and the second image as the WMn MPRAGE image.

2.2 Imaging equation

For an inversion recovery sequence repeated every T_R , at any voxel v , we can write:⁹

$$I(v) = M_{PD}(v) [1 - 2\exp(-T_I/M_{T1}(v)) + \exp(-T_R/M_{T1}(v))], \quad (1)$$

where $I(v)$ is the intensity of the image at v , $M_{PD}(v)$ is the value of the proton density map of the subject at v , T_I is the TI, $M_{T1}(v)$ is the value of the subject's T_1 map at v , and T_R is the TR. In our case, where we have two T1w images of the same subject with different TI, we can write two instances of the same equation, one for each image and with the corresponding TI. Doing so will result in a system of two nonlinear equations with two unknowns (M_{PD} , M_{T1}) at each voxel, which we can solve using least squares.

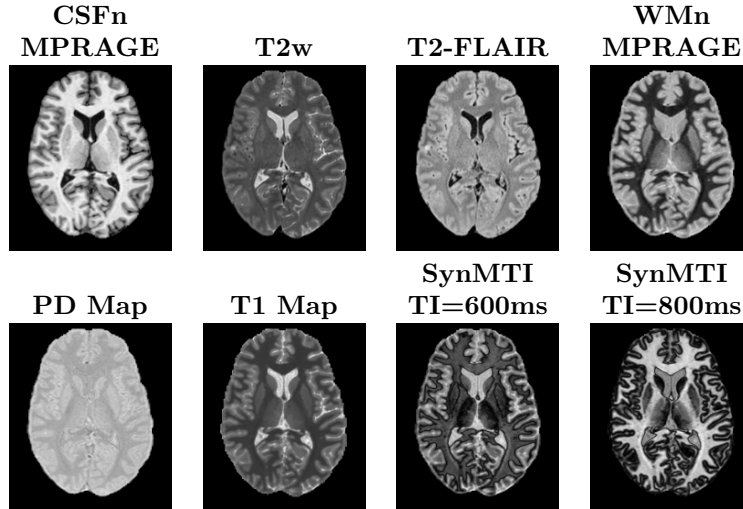


Figure 1. A slice of the preprocessed data and synthetic MTI images. The first row shows the contrast-weighted images directly measured from the subject, after preprocessing: The first three are inputs to the model, while the rightmost one is the desired output. The second row shows two quantitative parameter maps calculated from the two MPRAGE images (as described in Sec. 2.2) and two synthetic MTI (SynMTI) images generated using the procedure described in Sec. 2.3. All MR images shown in this paper correspond to the same slice of the same subject.

2.3 Preprocessing

Images were skull stripped using HD-BET,¹⁰ bias field corrected using N4 from the SimpleITK toolkit,¹¹ rigidly aligned with the MNI atlas using ANTs,¹² and intensity normalized using *intensity-normalization*.¹³ Due to the coupled nature of the two T1w images and our intent to use Eqn. 1 to extract the PD and T1 maps from them, the relative intensities of the two images had to be preserved throughout the preprocessing. Hence, the two preprocessing steps which transform the image intensities were performed on both images jointly and using the same transformations: 1) For bias field correction, we used the geometric mean of the two bias fields, and 2) for intensity normalization, we normalized the MPRAGE image and scaled the WMn MPRAGE using the same scaling factor. Next, we used Eqn. 1 and the two MPRAGE images to extract the PD and T1 maps. Specifically, if we define:

$$f(x, y; a, b) = x [1 - 2 \exp(-a/y) + \exp(-b/y)],$$

we approximately solved the following optimization problem at each foreground* voxel v :

$$(M_{PD}(v), M_{T1}(v)) = \arg \min_{(x, y) \in \mathbb{R}^{\geq 0} \times \mathbb{R}^{\geq 0}} (I_1(v) - f(x, y; T_{I1}, T_R))^2 + (I_2(v) - f(x, y; T_{I2}, T_R))^2,$$

where M_{PD} and M_{T1} are our estimates of the two parameter maps, $\mathbb{R}^{\geq 0}$ is the set of non-negative real numbers, \times is the cartesian product, I_1 and I_2 are the MPRAGE images with the corresponding inversion times T_{I1} and T_{I2} , respectively, and T_R is the repetition time[†].

2.4 U-Net

Proposed by Ronneberger et al.,¹⁴ U-Net is perhaps the most widely used neural network architecture for medical imaging applications. For this work, we used this architecture with the addition of an extra skip connection at the very top layer, similar to the work of Zhao et al.¹⁵ This extra skip connection was inspired by the observation that **in its absence, the model would output blurry images** with relatively low resolutions. Throughout this paper, we will refer to this architecture as the U-Net, with the extra skip connection being implicit.

*In background (non-brain) voxels, both parameter maps were set to zero.

†In the dataset we used for this work, the same repetition time was used for acquiring both MPRAGE images.

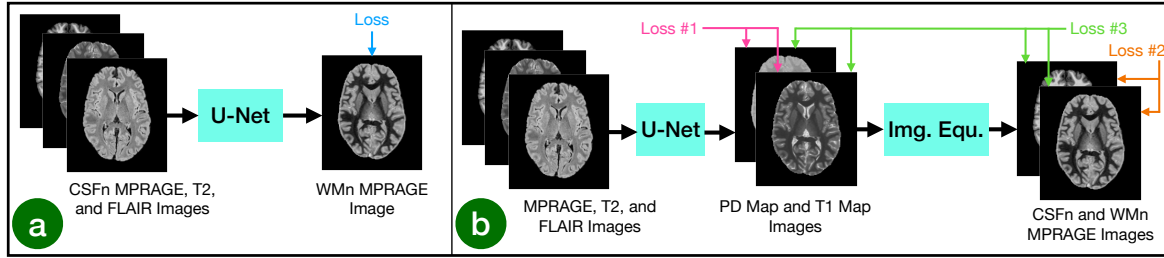


Figure 2. Methods covered in our experiments. Shown in (a) is Umapathy et al., while (b) shows both Moya-S  ez et al. and our proposed methods. Moya-S  ez et al. uses loss #1 (pink); while our training strategies 1 (S1) and 2 (S2) for the proposed method correspond to losses #2 (orange) and #3 (green), respectively. Arrows corresponding to each loss indicate which images were included in the total loss (see Eqn. 2).

2.5 ℓ_1 reconstruction loss

In this work, we used ℓ_1 reconstruction loss to train our models. This loss is defined as the voxel-wise sum of absolute difference between the target image and the synthesized image. Formally, if we have two images of the same size, $I(v)$ and $\hat{I}(v)$, the first one being the synthesis target and the second one being the result of the synthesis model, and $v \in V$ where v is any given voxel in the set of all image voxels V , the ℓ_1 reconstruction loss is:

$$\mathcal{L}_I = \mathcal{L}_{\ell_1}(I, \hat{I}) = \sum_{v \in V} |I(v) - \hat{I}(v)|.$$

2.6 Existing work and proposed approach

In our experiments, we compare our implementations of two previous works with our proposed method. All models are trained in a supervised manner with an ℓ_1 reconstruction loss (Sec. 2.5), with the input being the MPRAE, T2w, and T2-FLAIR images. The DL architecture we use for all methods is U-Net (Sec. 2.4). In the method of Umapathy et al.,⁷ the WMn MPRAE is directly synthesized from the other images. We train a similar model using our WMn MPRAE images as the output. Our implementation of Moya-S  ez et al.⁸ synthesizes the PD and T1 maps from the input images and is trained using the subjects' PD and T1 maps. Our proposed method also synthesizes the PD and T1 maps from the input images, but it passes them through Eqn. 1 to generate two synthetic images as output: a CSFn and a WMn MPRAE image. Specifically, the U-Net takes three 3D images as input (corresponding to the three input contrasts), and outputs two images of the same size, which are the model's estimates of the PD and T1 parameter maps (i.e., M_{PD} and M_{T1}) corresponding to the input images. Then, each synthetic MPRAE image is generated by passing M_{PD} and M_{T1} (the outputs of the U-Net) to the right-hand side of Eqn. 1 and plugging-in the corresponding T_R and T_I values, which are scalar acquisition parameters. Once the synthetic images are generated, one can compare them with the acquired ground truth images. Similarly, the parameter maps estimated by the U-Net can be compared with the parameter maps we had acquired by solving Eqn. 1 (as outlined in Sec. 2.3). These comparisons result in four loss terms, and the total loss with which the model is trained is a linear combination of these four terms. Under this framework, the total loss can be expressed as

$$\mathcal{L}_{\text{total}} = a \times \mathcal{L}_{\text{PDM}} + b \times \mathcal{L}_{\text{T1M}} + c \times \mathcal{L}_{\text{CSFn}} + d \times \mathcal{L}_{\text{WMn}}, \quad (2)$$

where \mathcal{L}_{PDM} and \mathcal{L}_{T1M} are the loss terms corresponding to the parameter maps, $\mathcal{L}_{\text{CSFn}}$ and \mathcal{L}_{WMn} are the loss terms corresponding to the synthetic MPRAE images, and a , b , c , and d are non-negative hyperparameters. We can immediately see that the the model proposed by Moya-S  ez et al. is a special case of this framework, where $a = b = 1$ and $c = d = 0$ in Eqn. 2.

In addition to our implementation of the work of Moya-S  ez et al., we train two other versions of this model using two strategies: 1) supervised with the two MPRAE images in an end-to-end fashion ($a = b = 0$ and $c = d = 1$ in Eqn. 2), and 2) supervised with the PD and T1 maps as well as the two MPRAE images ($a = b = c = d = 1$ in Eqn. 2). The methods are shown in Fig. 2.

Table 1. WMn MPRAGE PSNR (*db*) for test subjects and their corresponding mean and standard deviation (SD).

Method	Subj. #1	Subj. #2	Subj. #3	Mean(\pm SD)
Umapathy et al.	28.47	28.09	27.63	28.06(\pm 0.35)
Moya-Sáez et al.	28.32	25.97	26.90	27.07(\pm 0.97)
Proposed method – Strategy 1	28.84	28.66	27.82	28.44 (\pm 0.44)
Proposed method – Strategy 2	28.71	28.38	27.65	28.24(\pm 0.44)

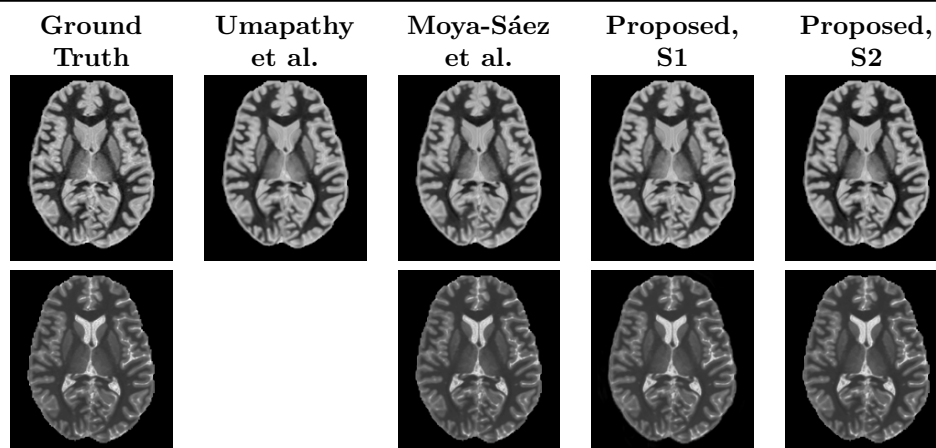


Figure 3. A slice of WMn MPRAGE images (top) and T1 maps (bottom) for a test subject. The first image is the ground truth and the rest are outputs of the models. Two notes: 1) Umapathy et al.⁷ does not generate T1 maps (this is an advantage of our proposed methods over the work of Umapathy et al.), and 2) Proposed method, S1 was only trained on contrast-weighted images and not T1 maps (this is an advantage of our model over the one proposed by Moya-Sáez et al.).

2.7 Segmenting thalamic nuclei

As part of our experiments, and to evaluate the output of the different models, we segment thalamic nuclei using the thalamus optimized multi atlas segmentation (THOMAS)¹⁶ software. The input to this software is a single MR image, which can either be a WMn MPRAGE or a CSFn MPRAGE. According to the original THOMAS paper, the results are expected to be more accurate when using a WMn MPRAGE, compared to using a CSFn one.

3. EXPERIMENTS

We withheld three test subjects from our 18 and divided the remaining 15 subjects into three cross validation folds of 10 training and 5 validation subjects. For each method, we trained **three instances of the model** on the training data for each fold and used the voxel-wise median output of the three networks as output. We first report peak signal-to-noise ratio (PSNR) for each method in Table 1 with example outputs in Fig. 3. To show the effectiveness of the synthetic images in downstream tasks, we then segmented the thalamic nuclei using THOMAS (described in Sec. 2.7). We ran THOMAS six times per test subject: Once using the acquired WMn MPRAGE as input, once using the acquired CSFn MPRAGE as input, and four times using the synthetic WMn MPRAGE images (once for each of the four methods). Su et al.¹⁶ report superior performance on the WMn MPRAGE over the CSFn MPRAGE; as such we applied THOMAS to the acquired **WMn MPRAGE image as a reference**, and **calculated the Sørensen–Dice coefficient (“Dice score”) between the reference segmentation mask and each of the other five segmentation results**. Mean Dice scores (and their standard deviations) are reported in Table 2 and sample segmentation results are shown in Fig. 4.

4. DISCUSSION AND CONCLUSIONS

We proposed a novel method to synthesize WMn MPRAGE images. Our method improves upon existing methods, as 1) it can be trained using exclusively contrast-weighted images, and 2) it jointly extracts parameter maps

Table 2. Mean(\pm SD) Dice scores for the thalamic nuclei segmentation experiment (explained in Sec. 3). The rows (excluding the last row) are sorted according to average volume in the reference segmentation (reported in the unit of voxels in the second column). The last row shows a weighted average of the scores of all the other rows, weighed by their average volume. The abbreviations in the first column correspond to the following: From the medial group: habenula (Hb), mediodorsal (MD), and centromedian (CM). From the posterior group: medial geniculate nucleus (MGN), lateral geniculate nucleus (LGN), and pulvinar (Pul). From the lateral group: ventral posterolateral (VPL), ventral lateral posterior (VLP), ventral lateral anterior (VLa), and ventral anterior nucleus (VA). From the anterior group: anteroventral (AV). Finally, THOMAS also segments the mammillothalamic tract (MTT), which we have also included in the table.¹⁶

Structure	\downarrow Vol.	Umapathy et al.	Moya-Sáez et al.	Ours, S1	Ours, S2	CSFn
Pul	5219	0.89(\pm 0.05)	0.92(\pm 0.02)	0.91(\pm 0.03)	0.93(\pm0.02)	0.89(\pm 0.02)
VLP	3090	0.87(\pm 0.06)	0.88(\pm 0.03)	0.87(\pm 0.07)	0.91(\pm0.02)	0.69(\pm 0.15)
MD	2275	0.88(\pm 0.10)	0.94(\pm0.01)	0.94(\pm0.00)	0.94(\pm0.00)	0.81(\pm 0.08)
VA	1032	0.81(\pm 0.11)	0.85(\pm 0.02)	0.83(\pm 0.08)	0.88(\pm0.01)	0.59(\pm 0.12)
VPL	972	0.75(\pm 0.09)	0.81(\pm 0.04)	0.75(\pm 0.10)	0.84(\pm0.08)	0.70(\pm 0.14)
CM	412	0.79(\pm 0.12)	0.87(\pm 0.01)	0.88(\pm0.00)	0.87(\pm 0.00)	0.68(\pm 0.14)
AV	322	0.78(\pm 0.12)	0.86(\pm0.01)	0.85(\pm 0.02)	0.85(\pm 0.01)	0.75(\pm 0.04)
MGN	265	0.78(\pm 0.17)	0.90(\pm0.01)	0.88(\pm 0.02)	0.89(\pm 0.01)	0.84(\pm 0.03)
LGN	213	0.59(\pm 0.22)	0.69(\pm 0.05)	0.67(\pm 0.12)	0.73(\pm0.06)	0.61(\pm 0.07)
VLa	174	0.56(\pm 0.15)	0.64(\pm 0.04)	0.62(\pm 0.06)	0.71(\pm0.02)	0.25(\pm 0.16)
MTT	107	0.60(\pm 0.24)	0.78(\pm0.03)	0.75(\pm 0.02)	0.78(\pm0.03)	0.53(\pm 0.03)
Hb	32	0.66(\pm 0.13)	0.65(\pm 0.04)	0.64(\pm 0.08)	0.70(\pm0.09)	0.53(\pm 0.05)
Aggregated	—	0.85(\pm 0.08)	0.89(\pm 0.01)	0.88(\pm 0.02)	0.91(\pm0.01)	0.77(\pm 0.08)

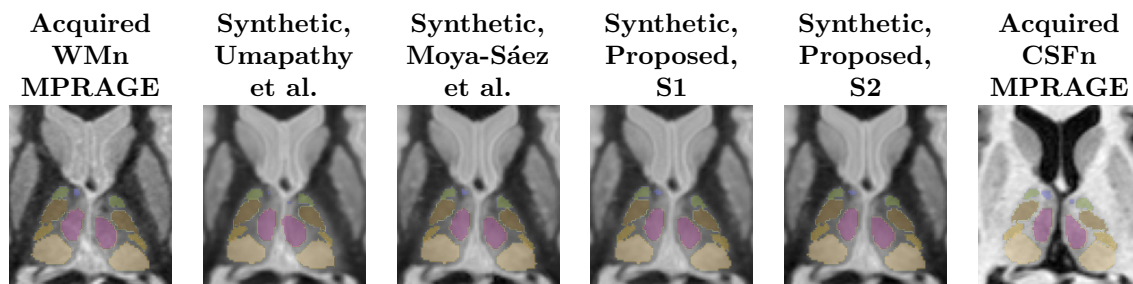


Figure 4. A cropped slice of the results from our segmentation experiments, overlaid on the image from which the segmentation was calculated and zoomed in on the thalamus. The first and last MR images (also shown in Fig. 1) were acquired and the rest (also shown in Fig. 3) are synthetic.

from the images, during both training and prediction. For our first experiment, we demonstrated that the model has superior performance compared to the previously existing methods on our limited cohort. This can be seen in Table 1. We also showed in Fig. 3 that our model outputs WMn MPRAGE images and T1 maps that are visually almost identical to the ground truth. We performed a second experiment, which demonstrated that the results of our model can be used to segment thalamic nuclei, as can be seen in Table 2 and Fig. 4. We can also see from Table 2 that the segmentation obtained by using the synthetic WMn MPRAGE is more similar to the segmentation obtained by using the acquired WMn MPRAGE, than the segmentation obtained using the acquired CSFn MPRAGE is. This implies that if one aims to segment thalamic nuclei, in the absence of an acquired WMn MPRAGE image, using a synthetic WMN MPRAGE image generated from our model is preferable to using the acquired CSFn MPRAGE image. In the future, we think exploring whether learning based thalamic nuclei parcellation^{17–19} algorithms can benefit through retraining or optimization of the selected MTI used during training.

ACKNOWLEDGMENTS

This work was supported in part by the Intramural Research Program of the NIH, National Institute on Aging, and the National Institute of Neurological Disorders and Stroke under grant R01-NS105503 (PI: R.P. Gullapalli).

REFERENCES

- [1] Sherman, S. M. and Guillery, R. W., [*Exploring the thalamus*], Elsevier (2001).
- [2] Zhuo, J. et al., “Visualization of the VIM Thalamic Nucleus using Synthesized MPRAGE Images,” in [*Annals 25th Annual Meeting ISMRM*], (2017).
- [3] Sudhyadhom, A. et al., “A high resolution and high contrast MRI for differentiation of subcortical structures for DBS targeting: FGATIR,” *NeuroImage* **47**, T44–T52 (2009).
- [4] Tourdias, T. et al., “Visualization of intra-thalamic nuclei with optimized white-matter-nulled MPRAGE at 7T,” *NeuroImage* **84**, 534–545 (2014).
- [5] Bobman, S. A. et al., “Cerebral magnetic resonance image synthesis,” *American Journal of Neuroradiology* **6**(2), 265–269 (1985).
- [6] Ji, S., Yang, D., Lee, J., Choi, S. H., Kim, H., and Kang, K. M., “Synthetic MRI: technologies and applications in neuroradiology,” *Journal of Magnetic Resonance Imaging* **55**(4), 1013–1025 (2022).
- [7] Umapathy, L. et al., “Convolutional Neural Network Based Frameworks for Fast Automatic Segmentation of Thalamic Nuclei from Native and Synthesized Contrast Structural MRI,” *Neuroinformatics* **20**(3), 1–14 (2021).
- [8] Moya-Sáez et al., “A deep learning approach for synthetic MRI based on two routine sequences and training with synthetic data,” *Computer Methods and Programs in Biomedicine* **210**, 106371 (2021).
- [9] Hornak, J. P., [*The basics of MRI*], Rochester Institute of Technology (2006).
- [10] Isensee, F. et al., “Automated brain extraction of multisequence MRI using artificial neural networks,” *Human Brain Mapping* **40**(17), 4952–4964 (2019).
- [11] Tustison, N. J. et al., “N4ITK: Improved N3 Bias Correction,” *IEEE Transactions on Medical Imaging* **29**(6), 1310–1320 (2010).
- [12] Avants, B. B. et al., “Advanced normalization tools (ANTs),” *Insight J* **2**(365), 1–35 (2009).
- [13] Reinhold, J. C. et al., “Evaluating the impact of intensity normalization on MR image synthesis,” in [*Medical Imaging 2019: Image Processing*], **10949**, 890–898, SPIE (2019).
- [14] Ronneberger, O. et al., “U-Net: Convolutional Networks for Biomedical Image Segmentation,” in [*MICCAI 2015*], **9351**, 234–241, Springer (2015).
- [15] Zhao, C. et al., “Whole Brain Segmentation and Labeling from CT Using Synthetic MR Images,” in [*Machine Learning in Medical Imaging*], **10541**, 291–298, Springer International Publishing (2017).
- [16] Su, J. H. et al., “Thalamus Optimized Multi Atlas Segmentation (THOMAS): Fast, fully automated segmentation of thalamic nuclei from structural MRI,” *NeuroImage* **194**, 272–282 (2019).
- [17] Feng, A. et al., “Label propagation via random walk for training robust thalamus nuclei parcellation model from noisy annotations,” in [*20th International Symposium on Biomedical Imaging (ISBI 2023)*], (2023).
- [18] Stough, J. V. et al., “Automatic method for thalamus parcellation using multi-modal feature classification,” in [*17th International Conference on Medical Image Computing and Computer Assisted Intervention (MICCAI 2014)*], *Lecture Notes in Computer Science* **8675**, 169–176, Springer Berlin Heidelberg (2014).
- [19] Yan, C. et al., “Segmenting thalamic nuclei from manifold projections of multi-contrast MRI,” in [*Proceedings of SPIE Medical Imaging (SPIE-MI 2023)*, San Diego, CA, February 19 – 23, 2023], (2023).